Nanoscale

PAPER

View Article Online
View Journal | View Issue

Cite this: *Nanoscale*, 2016, **8**, 2832

Characterization of multifunctional β-$NaEuF_4$/$NaGdF_4$ core–shell nanoparticles with narrow size distribution†

Lilli Schneider,*[a] Thorben Rinkel,[b] Benjamin Voß,[b] Artur Chrobak,[c] Johann P. Klare,[a] Jan Neethling,[d] Jaco Olivier,[d] Dominik Schaniel,[e] El-Eulmi Bendeif,[e] Federica Bondino,[f] Elena Magnano,[f] Igor Píš,[f,g] Kamil Balinski,[a] Joachim Wollschläger,[a] Heinz-Jürgen Steinhoff,[a] Markus Haase[b] and Karsten Kuepper*[a]

The properties of β-$NaEuF_4$/$NaGdF_4$ core–shell nanocrystals have been thoroughly investigated. Nanoparticles with narrow size distribution and an overall diameter of ~22 nm have been produced with either small β-$NaEuF_4$ cores (~3 nm diameter) or large β-$NaEuF_4$ cores (~18 nm diameter). The structural properties and core–shell formation are investigated by X-ray diffraction, transmission electron microscopy and electron paramagnetic resonance, respectively. Optical luminescence measurements and X-ray photoelectron spectroscopy are employed to gain information about the optical emission bands and valence states of the rare earth constituents. Magnetic characterization is performed by SQUID and X-ray magnetic circular dichroism measurements at the rare earth $M_{4,5}$ edges. The characterization of the core–shell nanoparticles by means of these complementary techniques demonstrates that partial intermixing of core and shell materials takes place, and a significant fraction of europium is present in the divalent state which has significant influence on the magnetic properties. Hence, we obtained a combination of red emitting Eu^{3+} ions and paramagnetic Gd^{3+} ions, which may be highly valuable for potential future applications.

Received 6th October 2015,
Accepted 27th December 2015

DOI: 10.1039/c5nr06915g

www.rsc.org/nanoscale

1 Introduction

$NaREF_4$ nanoparticles (RE: rare earth) have attracted increasing interest in recent years for applications in biological labeling and imaging,[1–20] photodynamic therapy and drug delivery,[21–26] photovoltaics,[27–30] photonics[31–33] and security labeling.[34–36] Frequently, nanocrystals with core–shell structure are synthesized, since a shell of inert material increases the quantum yield of a luminescent particle core by decreasing energy losses on the particle surface.[37–39] Particles containing one or more shells of the doped material furthermore allow us to spatially separate the dopant ions with different functionalities and to control the migration of energy within such structures.[40–49] For lanthanide ions emitting in the red and near infrared spectral regions, fluoride host materials are of particular interest because the very low phonon frequencies of fluoride lattices decrease the probabilities of multiphonon relaxation processes, resulting in high quantum yields. One example is the Eu^{3+} ion, displaying pure red emission in many host materials, because all transitions except those from the $^5D_0$ level are quenched due to multiphonon relaxation. In the fluoride host, however, also transitions from the higher $^5D_1$, $^5D_2$ and $^5D_3$ levels are observed provided that the concentration of the Eu^{3+} dopant is low. At higher concentrations, however, cross-relaxation between adjacent Eu^{3+} in the lattice leads to quenching of the $^5D_1$, $^5D_2$ and $^5D_3$ transitions in these materials, too. Trivalent gadolinium, on the other hand, is characterized by a relatively large energy gap between the ground state ($^8S_{7/2}$) and the lowest excited level ($^6P_{7/2}$).[21] Importantly, this excited level is situated in the ultraviolet spectral

[a]*Department of Physics, Center of Physics and Chemistry of New Materials, Universität Osnabrück, Barbarastr. 7, 49076 Osnabrück, Germany. E-mail: lischroe@uos.de, kkuepper@uos.de*
[b]*Institute of Chemistry of New Materials, Center of Physics and Chemistry of New Materials, Universität Osnabrück, Barbarastr. 7, 49076 Osnabrück, Germany*
[c]*Institute of Physics, Silesian University, Uniwersytecka 4, 40-007 Katowice, Poland*
[d]*Centre for HRTEM, Nelson Mandela Metropolitan University, P.O. Box 77000, Port Elizabeth, South Africa*
[e]*Université de Lorraine, CRM2, UMR 7036, Vandoeuvre-les-Nancy, F-54506, France*
[f]*IOM CNR, Laboratorio TASC, S.S. 14 km 163.5, 34149 Basovizza, Trieste, Italy*
[g]*Elettra-Sincrotrone Trieste S.C.p.A., S.S. 14 km 163.5, 34149 Basovizza, Trieste, Italy*

†Electronic supplementary information (ESI) available. See DOI: 10.1039/C5NR06915G

region, *i.e.* well above the emitting $^5D_0$, $^5D_1$, $^5D_2$ and $^5D_3$ levels of Eu^{3+}. A $NaGdF_4$ shell around a $NaEuF_4$ core can therefore improve the luminescence efficiency of the core. Moreover, the lattice mismatch between the core and the shell is very low due the very similar lattice constants of $NaGdF_4$ and $NaEuF_4$. In addition to their interesting optical properties, europium and gadolinium have remarkable magnetic properties. Owing to their seven unpaired electrons, Gd^{3+} ions in the ground state can, for instance, efficiently alter the relaxation times of the surrounding water protons and are therefore the basis of the most commonly used contrast agents in magneto resonance imaging.[50] While gadolinium ions usually form the oxidation state III+, europium compounds can contain either Eu^{3+} or Eu^{2+} ions, or both. Trivalent europium in the ground state ($^7F_0$, $S = 3$, $L = 3$, $J = 0$) has no magnetic moment while divalent europium has seven unpaired electrons in the ground state ($^8S_{7/2}$, $S = 8$, $L = 0$, $J = 7/2$). Interestingly in some trivalent compounds formation of divalent europium states on the surface was observed.[51,52] Moreover, Kachkanov *et al.* detected an optically induced magnetic moment of Eu^{3+} ions in GdN.[53]

In this work, we synthesized core–shell systems composed of a β-$NaEuF_4$ core and a β-$NaGdF_4$ shell. This structure has two advantages. Firstly, the influence of different surrounding media on the β-$NaEuF_4$ core can be minimized or entirely removed. Secondly, the combination of red emitting Eu^{3+} ions and paramagnetic Gd^{3+} ions is highly valuable.

The nominal size is the expected size based on the used materials respectively precursor particles. We use a number of complementary methods to evaluate the structure of β-$NaEuF_4$/$NaGdF_4$ core–shell particles and to study their electronic and magnetic properties. Detailed knowledge of these properties is indispensable to compare the results with those of Eu^{3+} doped β-$NaGdF_4$ nanoparticles and to further optimize the core–shell system in question. Structural properties and core–shell formation are determined by means of X-ray powder diffraction (XRD) and high resolution transmission electron microscopy (HR-TEM). Core–shell formation is further investigated by electron paramagnetic resonance (EPR) and optical luminescence spectroscopy. Chemical and electronic properties with special emphasis on the Eu and Gd valence states are determined employing X-ray photoelectron spectroscopy (XPS), whereas magnetic characterization is performed with a superconducting quantum interference device (SQUID) magnetometer. The measured magnetization curves are analyzed by means of Monte Carlo based Heisenberg simulations. Finally we performed element specific X-ray magnetic circular dichroism (XMCD) at the Eu $M_{4,5}$ and Gd $M_{4,5}$ edges to gain a complete picture of the internal magnetic structure of the multifunctional β-$NaEuF_4$/$NaGdF_4$ core–shell nanoparticles.

2 Results and discussion

2.1 Total scattering measurement and PDF analysis

Fig. 1 shows the pair distribution functions (PDFs) for both core–shell samples as well as the 22 nm β-$NaGdF_4$ nanocrystals doped with 1% Eu. The two samples containing low Eu and high Gd concentration (20 nm β-$NaEuF_4$/$NaGdF_4$ core–shell nanoparticles (NPs) with a 3 nm β-$NaEuF_4$ core, 22 nm β-$NaGdF_4$ nanoparticle (NP) doped with 1% Eu) exhibit very similar PDFs that differ significantly from the core–shell sample with the 18 nm β-$NaEuF_4$ core. Comparing the two core–shell samples (20 nm β-$NaEuF_4$/$NaGdF_4$ core–shell nanoparticles with a 3 nm β-$NaEuF_4$ core, 22 nm β-$NaEuF_4$/$NaGdF_4$ core–shell nanoparticles with an 18 nm β-$NaEuF_4$ core) we can clearly identify shifts of the peak positions in the PDF (corresponding to atom–atom distances). Note that the structures of bulk β-$NaEuF_4$ and β-$NaGdF_4$ are quite similar and the differences in bond distances between the different atoms are thus expected to be small. In order to enhance the visibility of the structural differences we calculated the differences between the corresponding PDFs, given as $\Delta G(r)$ in Fig. 1. One can clearly see that the difference between the PDF of the 20 nm β-$NaEuF_4$/$NaGdF_4$ core–shell nanoparticles with a 3 nm β-$NaEuF_4$ core and the 22 nm β-$NaGdF_4$ NP doped with 1% Eu is very small, resulting in very weak features in the $\Delta G(r)$. A core–shell nanoparticle with a small β-$NaEuF_4$ core thus exhibits almost the same structure as a nanoparticle doped with 1% Eu, indicating that the structural relaxation is similar for these two cases. In other words, from the PDF analysis alone it is impossible to distinguish between the structure of the core–shell NP and a homogeneously doped NP. In contrast, the difference of the two PDFs ($\Delta G(r)$) of the two core–shell samples is much more pronounced. Almost all peak positions are affected and the shifts are more pronounced for larger atom–atom distances r. In order to investigate this result in more detail we performed simulations of the PDFs based on pure crystalline, spherical 22 nm β-$NaGdF_4$ and β-$NaEuF_4$ nanocrystals. The results are shown in Fig. 2. The distances are slightly shorter in the β-$NaGdF_4$ nanoparticle as expected from the smaller lattice parameters. We observe a good agreement between the simulated peak positions in the PDF for the

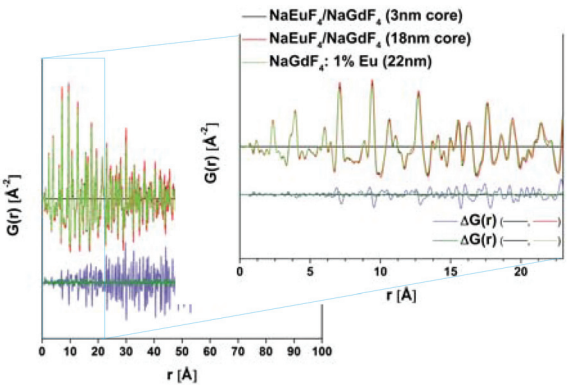

Fig. 1 Comparison of atomic PDFs in real space, $G(r)$ for 20 nm β-$NaEuF_4$/$NaGdF_4$ core–shell nanoparticles with a 3 nm β-$NaEuF_4$ core and ~8.5 nm β-$NaGdF_4$ shell, 22 nm β-$NaEuF_4$/$NaGdF_4$ core–shell nanoparticles (NPs) with an 18 nm β-$NaEuF_4$ core and 22 nm β-$NaGdF_4$ nanoparticle (NP) doped with 1% Eu and their differential PDFs.

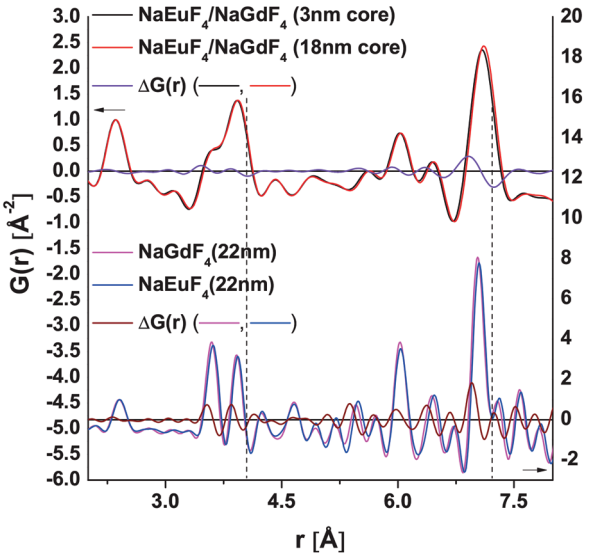

Fig. 2 Comparison of observed PDFs for 20 nm β-$NaEuF_4$/$NaGdF_4$ core–shell nanoparticles with a 3 nm β-$NaEuF_4$ core and ~8.5 nm β-$NaGdF_4$ shell and 22 nm β-$NaEuF_4$/$NaGdF_4$ core–shell NPs with an 18 nm β-$NaEuF_4$ core and calculated PDFs of 22 nm β-$NaGdF_4$ and β-$NaEuF_4$ spheres with the corresponding differential PDFs (spectra are normalized to the first peak).

two pure nanoparticles and the experimentally determined PDF. The peaks are broader in the experimental PDF, which is due to a lower resolution of the experiment, but also due to the fact that in the core–shell nanoparticles we expect some strain and defects as well as a not perfectly spherical shape. We don't expect a significant impact of the particle-size distribution on the PDF since the size distributions are rather narrow, *e.g.*, the β-$NaEuF_4$/$NaGdF_4$ (3 nm core) nanoparticles exhibit a size distribution of 16.8 nm ± 5% (see Table 1), corresponding to particles ranging from 16 nm to 17.7 nm. If the structural difference (*e.g.* distances between first neighbours) between two such nanoparticles is well below the resolution of 0.138 Å, there will be no visible effect on the experimental PDF. For illustration one can compare the two simulated PDFs for the 22 nm β-$NaGdF_4$ and β-$NaEuF_4$ particles given in Fig. 2, where the difference in the first neighbour distances between the pure Gd and the pure Eu sample is of the order of 0.02 Å, which is at the limit of visibility in the $G(r)$. Structural differences between two identical nanoparticles differing only by 5% in size would therefore not be detected in the experiment. As a first conclusion we can state that a β-$NaEuF_4$/$NaGdF_4$ core–shell nanoparticle with a 3 nm β-$NaEuF_4$ core exhibits approximately the same structure as a slightly Eu-doped β-$NaGdF_4$ nanoparticle and its main structural parameters are those of the β-$NaGdF_4$ structure. β-$NaEuF_4$/$NaGdF_4$ core–shell nanoparticles with an 18 nm β-$NaEuF_4$ core on the other hand resemble the corresponding pure β-$NaEuF_4$ structure. Due to the limited resolution of the experiment a more detailed modelling, *e.g.* to investigate the core–shell interface, is currently not possible. High-resolution electron microscopy investigations were carried out for further characterisation of the nanoparticles.

Table 1 Sample label, nominal size and size distribution determined by transmission electron microscopy (TEM) analysis (Fig. S2 and S4)

Samples	Nominal size	Size (from TEM)
$NaEuF_4$/$NaGdF_4$ (3 nm core)	20 nm	16.8 nm ± 5%
$NaEuF_4$/$NaGdF_4$ (18 nm core)	22 nm	23 nm ± 3.8%
$NaGdF_4$:1% Eu	22 nm	25.4 nm ± 4%
$NaEuF_4$ (3 nm)	3 nm	Not evaluable
$NaEuF_4$ (18 nm)	18 nm	19.7 nm ± 4.2%
$NaGdF_4$/$NaEuF_4$ (3 nm core)	20 nm	20.2 nm ± 3.9%
$NaEuF_4$:1% Gd	22 nm	24.5 nm ± 5.4%
$NaGdF_4$ (3 nm)	3 nm	Not evaluable
$NaGdF_4$ (22 nm)	22 nm	25.6 nm ± 5.8%

2.2 TEM-HRTEM

The morphology of the nanoparticles was characterized by transmission electron microscopy (TEM). It can be seen that the particles are nearly spherical or slightly elongated and retain the initial morphology of the precursor core particles (Fig. 3). Inter-planar spacings were measured using fast Fourier transform (FFT) analysis of the HRSTEM images. Inter-planar spacings with distances 0.29 nm, 0.18 nm and 0.16 nm were measured. These match very closely to the theoretical values for the (1,1,0), (0,0,2) and (1,1,2) planes respectively. Because the lattice constants between the core and the shell are similar, no significant differences are observed. Fig. 4(a)

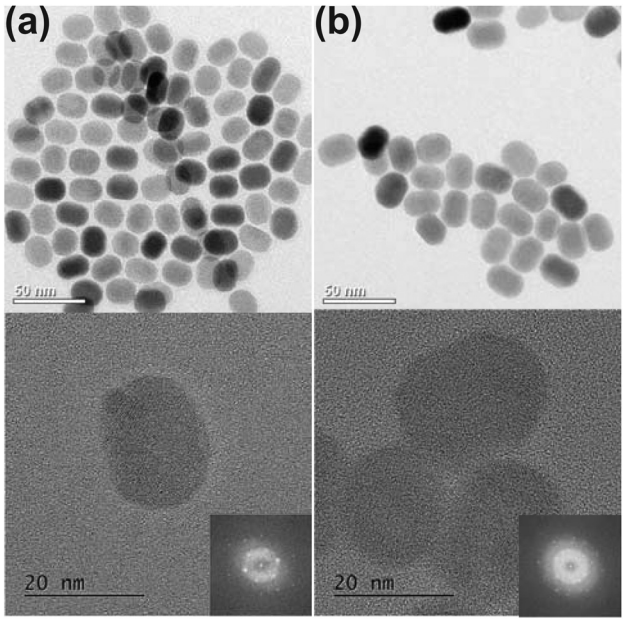

Fig. 3 TEM images showing (top) general morphology and (bottom) high-resolution images of the (a) 18 nm β-$NaEuF_4$ NP and (b) 22 nm β-$NaEuF_4$/$NaGdF_4$ NP with a 2 nm β-$NaGdF_4$ shell around the 18 nm β-$NaEuF_4$ core. The insets show the fast Fourier transforms (FFTs) of HR-TEM images.

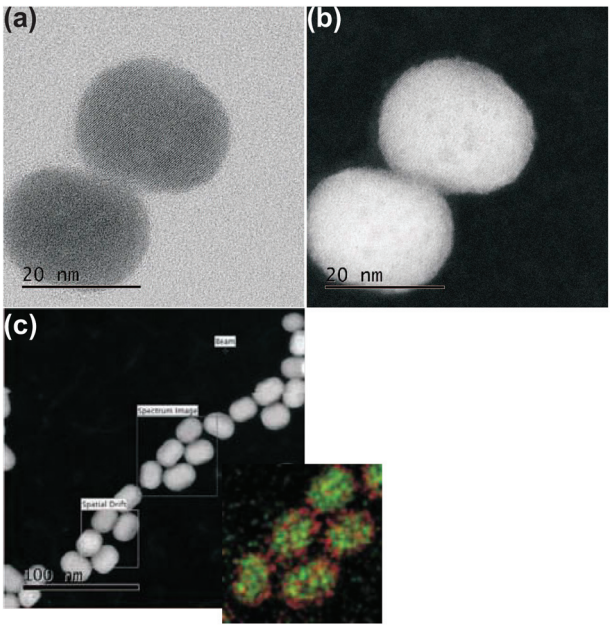

Fig. 4 High resolution scanning transmission electron microscopy bright field (HRSTEM-BF) image of (a) 22 nm β-$NaEuF_4$/$NaGdF_4$ core–shell NPs with an 18 nm β-$NaEuF_4$ core and 2 nm β-$NaGdF_4$ shell and (b) the corresponding high-angle annular dark field (HAADF) high resolution scanning transmission electron microscope (HRSTEM) image. And (c) scanning transmission electron microscope-electron energy loss spectroscopy (STEM-EELS) survey image and colour map of Eu (green) and Gd (red).

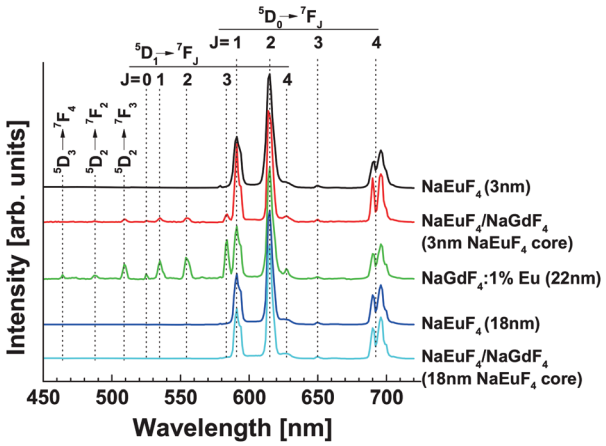

Fig. 5 Normalized emission spectra of 3 nm β-$NaEuF_4$, 20 nm β-$NaEuF_4$/$NaGdF_4$ NPs with a 3 nm core, 22 β-$NaGdF_4$ NP doped with 1% Eu, 18 nm β-$NaEuF_4$ and 22 nm β-$NaEuF_4$/$NaGdF_4$ NPs with an 18 nm β-$NaEuF_4$ core. The spectra were recorded under 394 nm excitation of the Eu^{3+} ions ($^7F_{0,1} \rightarrow {}^5L_6$). All particles consist of hexagonal phase (β-phase).

shows the high-resolution bright field scanning transmission electron microscopy (BF STEM) images of the core–shell nanoparticles with an 18 nm β-$NaEuF_4$ core and a 2 nm β-$NaGdF_4$ shell and (b) the corresponding high-angle annular dark field (HAADF) image.

The HAADF HRSTEM image of the 22 nm β-$NaEuF_4$/$NaGdF_4$ core–shell NPs with an 18 nm β-$NaEuF_4$ core and 2 nm β-$NaGdF_4$ shell in Fig. 4(b) does not show significant variation within the nanoparticle.

The STEM-EELS mapping of the 22 nm β-$NaEuF_4$/$NaGdF_4$ core–shell NPs with an 18 nm β-$NaEuF_4$ core and 2 nm β-$NaGdF_4$ shell (Fig. 4(c)) shows according to the colour map (inset) evidence of a core shell structure with Eu (green) in the center and Gd (red) on the surface.

2.3 Luminescence

The optical properties of the β-$NaEuF_4$ core and β-$NaEuF_4$/$NaGdF_4$ core–shell nanocrystals were studied by photoluminescence spectroscopy. As expected, excitation at the $^7F_{0,1} \rightarrow {}^5L_6$ transition of Eu^{3+} at ~394 nm results in Eu^{3+} emission for all nanoparticles containing Eu^{3+} ions (Fig. 5). In all cases the highest emission intensities are recorded at ~591, 614 and 696 nm corresponding to the $^5D_0 \rightarrow {}^7F_1$, $^5D_0 \rightarrow {}^7F_2$ and $^5D_0 \rightarrow {}^7F_4$ intra-4f shell transitions of Eu^{3+} respectively.[54] These transitions are characteristic for luminescent materials containing Eu^{3+} ions and are, for instance, also observed for the β-$NaGdF_4$ nanocrystals doped with 1 mol% of Eu^{3+}. Fig. 5 shows, however, that the emission spectrum of such weakly doped particles displays additional lines between 450 nm and 580 nm, caused by transitions from the higher excited $^5D_3$, $^5D_2$ and $^5D_1$ levels of Eu^{3+} to its ^7F_J ground state multiplet. These emission lines are very weak in materials containing Eu^{3+} in high concentrations, since cross-relaxation between adjacent Eu^{3+} ions is known to quench the luminescence from these states. The $^5D_3$, $^5D_2$ and $^5D_1$ emission lines are therefore characteristic for Eu^{3+} ions having no Eu^{3+} neighbors in the crystal lattice and display negligible intensity, for instance, in the case of β-$NaEuF_4$ core particles (Fig. 5).[55,56] Fig. 5 shows, however, that after the formation of the $NaGdF_4$ shell, the $^5D_3$, $^5D_2$ and $^5D_1$ emission lines appear in the spectrum of the core–shell particles. This indicates that some Eu^{3+} ions are released from the β-$NaEuF_4$ core and incorporate into $NaGdF_4$ during formation of the shell. The figure also shows that the transitions from the higher ^5D states are much less intense for core–shell particles with 18 nm cores indicating that the number of Eu^{3+} ions released decreases with increasing core size. This observation is in accord with the lower surface-to-bulk ratio of 18 nm core particles compared to 3 nm core particles, since the release of Eu^{3+} ions should be proportional to the total surface area of all core particles. To further substantiate this result, we have investigated the core–shell particles containing Gd^{3+} by EPR spectroscopy.

2.4 Electron paramagnetic resonance spectroscopy

In general, the EPR spectrum of Gd^{3+} ions ($S = 7/2$) is characterized by the Zeeman interaction with a g-value ≈2 and exhibits significant contributions from zero-field splitting. The mean distance between two adjacent Gd^{3+} ions in the crystal lattice is reflected in the broadness of the EPR spectrum that

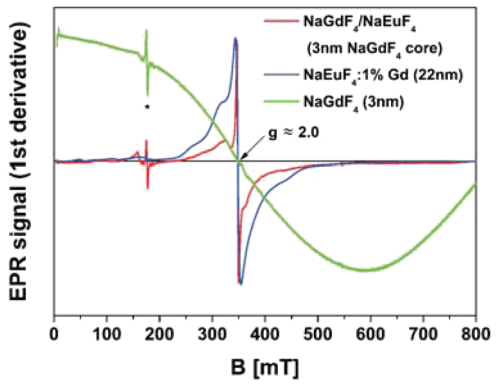

Fig. 6 Normalized EPR spectra of 20 nm core–shell particles composed of a 3 nm β-$NaGdF_4$ core and an ~8.5 nm β-$NaEuF_4$ shell (red), 22 nm β-$NaEuF_4$ NPs doped with 1% Gd (blue) and 3 nm β-$NaGdF_4$ precursor particles (green). Due to the large width of the EPR spectrum of the precursor particles it has a significantly lower intensity compared to the other spectra and consequently displays more noise when the spectra are normalized to the same signal height (scaling factors: blue, ×1; red, ×10; green, ×11). The asterisk denotes an impurity signal of the microwave cavity present in all spectra at 175 mT.

increases with increasing Gd concentration due to dipolar and isotropic exchange interactions between the ions, as observed in Fig. 6 for 3 nm β-$NaGdF_4$ particles (green spectrum).[57] A similar broadening due to Gd^{3+}–Gd^{3+} interactions has been observed for $NaYF_4$/$NaGdF_4$ core–shell nanocrystals, even if the shell of $NaGdF_4$ is as thin as 1 nm.[58] In the study presented here we investigated core–shell particles with significantly thicker shells, consisting of a small 3 nm β-$NaEuF_4$ core and an ~8.5 nm thick β-$NaGdF_4$ shell. Since the EPR signal of such particles would be fully dominated by the broad spectrum of the undiluted Gd^{3+} ions in the shell, we used core–shell nanocrystals with inverted composition in the EPR measurements, *i.e.*, 3 nm β-$NaGdF_4$ core particles with an ~8.5 nm β-$NaEuF_4$ shell. In Fig. 6, the EPR spectrum of these core–shell particles (red line) is compared with the EPR spectrum of β-$NaEuF_4$ nanocrystals doped with 1% Gd^{3+} (blue line) and the EPR spectrum of 3 nm β-$NaGdF_4$ core particles (green line). Note that all spectra are normalized at maximum signal height as indicated by the scaling factors given in the figure. The highest scaling factor was used for the $NaGdF_4$ core particles as the strong interaction of the Gd^{3+} ions in these particles leads to strong broadening of their EPR signal (green line). The lowest scaling factor was used in the spectrum of the weakly doped β-$NaEuF_4$:1% Gd particles. This spectrum exhibits a dominating narrow EPR signal (peak-to-peak width, $\Delta B_{pp} \approx 10$ mT) in the $g = 2$ region and additional contributions at higher g-values (lower magnetic fields), the latter indicating the presence of Gd^{3+} ions at sites with different symmetries and/or crystal fields compared to the bulk sites. Since we used rather large $NaEuF_4$:1% Gd particles with a diameter of 22 nm, the contribution from surface Gd^{3+} sites, however, is almost negligible in this case. The additional contributions therefore indicate that the Gd^{3+} dopant ions are not homogeneously distributed inside the particles as observed before.[58] Finally, the high scaling factor used for the β-$NaGdF_4$/$NaEuF_4$ core–shell nanocrystals shows that their EPR signal is much weaker than the signal of the doped β-$NaEuF_4$:1% Gd particles, although both samples contain europium and gadolinium in the same molar ratio of 99 to 1. The much lower intensity is in accord with the core shell structure, since the signal of the Gd^{3+} ions in the core is expected to be strongly broadened. Similar to the doped β-$NaEuF_4$:1% Gd particles, however, the normalized EPR spectrum of the core–shell particles also displays a narrow signal at $g \approx 2.0$ characteristic for isolated or weakly interacting Gd^{3+} ions. Since this signal is even narrower ($\Delta B_{pp} \approx 3$ mT) and of higher relative intensity compared to the doped β-$NaEuF_4$:1% Gd particles, it indicates the presence of highly diluted ($\ll$1%) Gd^{3+} ions in the β-$NaEuF_4$ shell. Komban *et al.* concluded from the EPR data for $NaYF_4$:Gd core–shell particles that the shell structure grows from dissolved precursor particles and that most likely also Y^{3+} ions are released from the surface of the core-precursors during the reaction.[58] The EPR data for the β-$NaGdF_4$:Eu core–shell particles shown in Fig. 6 indicates that these nanocrystals are formed in a similar way and therefore support the conclusions drawn above from luminescence spectroscopy.

2.5 Chemical properties, core level XPS

We employed core level XPS to investigate the chemical states of the Eu and Gd ions of the nanoparticles and core–shell systems in question. Fig. 7(a) displays the Gd 3d X-ray photoelectron spectra of the core–shell and pure β-$NaGdF_4$ (3 nm diameter) nanoparticles. The corresponding spectrum of a GdF_3 single crystal[52] is also shown for comparison. For all samples the Gd $3d_{5/2}$ and $3d_{3/2}$ core level binding energies are located at 1187.5 eV and 1219.5 eV, respectively. All the spectra show no distinct satellite features between the $3d_{5/2}$ and $3d_{3/2}$ main peaks indicating the absence of any metallic Gd contributions.[59]

Fig. 7(b)–(d) show the Eu 4d (and Gd 4d (Fig. 7(d))) spectra of pure β-$NaEuF_4$ (3 nm and 18 nm (Fig. 7(b) and (c))) and the β-$NaEuF_4$/$NaGdF_4$ core–shell nanoparticles with an 18 nm β-$NaEuF_4$ core (Fig. 7(d)). The Eu 4d XPS of the 3 nm β-$NaEuF_4$ nanoparticles comprises three distinct features located at 129.9 eV (A), 137.4 eV (B), and 143.4 eV (C). Features B and C can be attributed to the Eu^{3+} $4d_{5/2}$ and Eu^{3+} $4d_{3/2}$ states, whereas the lower binding energy peak A represents the Eu^{2+} $4d_{5/2}$ states,[52] whereas the Eu^{2+} $4d_{3/2}$ states are overlapping with the Eu^{3+} $4d_{5/2}$ states and not visible as distinct features in the corresponding Eu 4d spectra. We de-convolute these spectra using Gaussian/Lorentzian line profiles. In the case of the β-$NaEuF_4$/$NaGdF_4$ core–shell nanoparticles (18 nm β-$NaEuF_4$ core) this de-convolution approach is extended to the Gd^{3+} $4d_{5/2}$ and Gd^{3+} $4d_{3/2}$ states, assuming a pure trivalent Gd valence state in accordance with the results presented in Fig. 7(a). With the fitting approach described we are able to determine the Eu cation distribution of the nanoparticles investigated here. One can already see by the naked eye that the 3 nm β-$NaEuF_4$ nanoparticles comprise the highest

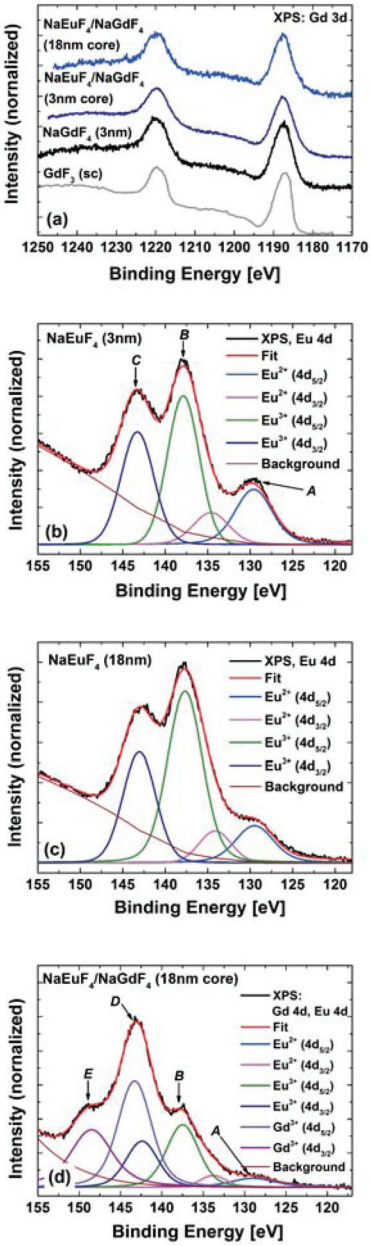

Fig. 7 Normalized XPS spectra of: (a) Gd 3d-core level of β-$NaEuF_4$/$NaGdF_4$ core–shell nanoparticles with 18 nm and 3 nm β-$NaEuF_4$ cores, 3 nm pure β-$NaGdF_4$ nanoparticles, and a GdF_3 single crystal[52] as a reference. (b) Eu 4d-core level of pure 3 nm β-$NaEuF_4$ nanoparticles, de-convoluted into Eu^{2+} and Eu^{3+} fractions. (c) Eu 4d-core level of pure 18 nm β-$NaEuF_4$ nanoparticles, de-convoluted into Eu^{2+} and Eu^{3+} fractions. (d) Eu 4d-core level of β-$NaEuF_4$/$NaGdF_4$ core–shell nanoparticles with an 18 nm β-$NaEuF_4$ core. Eu and Gd spectra are partly overlapping, and are de-convoluted into Eu^{2+}, Eu^{3+} and Gd^{3+} contributions.

amount of Eu^{2+} ions, we find the Eu valence state in this sample to be composed out of 30% Eu^{2+} and 70% Eu^{3+} ions. The Eu^{2+} fraction is significantly reduced for the other two samples, we find fractions of 20% Eu^{2+} for the 18 nm β-$NaEuF_4$ nanoparticles and 18% Eu^{2+} for the β-$NaEuF_4$/$NaGdF_4$ core–shell nanoparticles, respectively. We assume that this result can be likely due to the different surface to bulk ratios of the samples as the formation of divalent Eu should predominantly occur at the surface (interface) of the sample, since a similar effect has been reported by Burian *et al.* on different EuF_3 surfaces and interfaces.[52]

2.6 Electronic and magnetic properties

In order to elucidate further the magnetic properties all over the nanocrystals superconducting quantum interference device (SQUID) magnetometry measurements were performed.

Fig. 8(a) and (b) show thermomagnetic curves $M(T)$ of the precursor particles of pure β-$NaGdF_4$ and β-$NaEuF_4$ respectively. In the case of β-$NaGdF_4$ particles, the $M(T)$ dependences fulfill the Curie law but with small deviation that is clearly demonstrated in the $M \times T(T)$ curves. For pure Curie law (*i.e.* $M \sim 1/T$), the $M \times T(T)$ dependence should be a flat line, while the observed linear deviation indicates temperature independent component of magnetization which, in our case, can be attributed to some blocked magnetic moments of Gd. In the case of β-$NaEuF_4$ particles, the thermomagnetic curves are typical as for Eu^{3+} ions, showing the so-called van Vleck paramagnetism which is relatively weak and temperature independent. At low temperatures, below 20 K, traces of classical paramagnetic behavior are observed, *i.e.* sharp increase in magnetization with decreasing temperature. This effect is caused by an expected contribution of Eu^{2+} ions that pose magnetic moment and follow the Curie law. The possible origin of the Eu^{2+} presence is a surface valence transition, typical for nanoparticles containing Eu.

Fig. 8(c) shows hysteresis loops, determined at 2 K, for (i) pure β-$NaEuF_4$ and β-$NaGdF_4$ precursor particles, (ii) 22 nm β-$NaGdF_4$ nanocrystals doped with 1% of Eu and (iii) β-$NaEuF_4$/$NaGdF_4$ core–shell particles. Generally, the β-$NaEuF_4$ samples (3 nm and 18 nm) are paramagnetic. However, for the β-$NaEuF_4$ 3 nm nanocrystals some saturated component is detected which confirms the presence of magnetic Eu^{2+} ions. This answers the expectation of Eu^{2+} formation on the surface, consequently due to the large bulk to surface ratio in the 18 nm nanocrystals no signal is detectable. The pure β-$NaGdF_4$ precursor particles, β-$NaEuF_4$/$NaGdF_4$ core–shell particles with the 18 nm β-$NaEuF_4$ core and 22 nm β-$NaGdF_4$ nanocrystals doped with 1% Eu are paramagnetic with saturation magnetization as expected from the literature.[60] Surprisingly the β-$NaEuF_4$/$NaGdF_4$ core–shell nanocrystals with the 3 nm core show a butterfly shaped hysteresis loop. A similar behavior was recently found in rare earth based single molecular magnets.[61] The explanation of the hysteresis loop for the β-$NaEuF_4$/$NaGdF_4$ core–shell particles with the 3 nm β-$NaEuF_4$ core can be some magnetic anisotropy. Accounting the fact that for 22 nm β-$NaGdF_4$ and 3 nm β-$NaGdF_4$ samples the effect of hysteresis broadening was not observed one may propose a model in which the anisotropy exists at the interface between a magnetic shell and a non-magnetic core.

In order to confirm this hypothesis Monte Carlo simulations were performed. The simulations are based on the Heisenberg model and the so-called simulated annealing, as

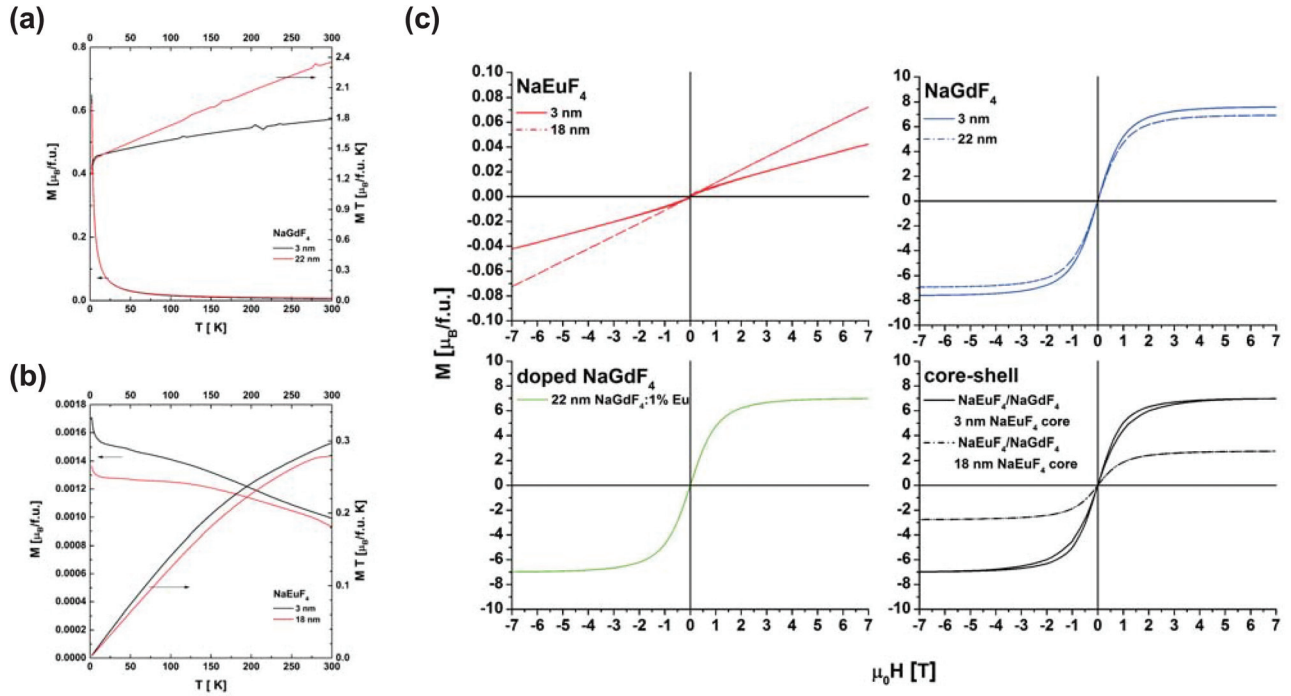

Fig. 8 Thermomagnetic $M(T)$ curves measured in $\mu_0 H$ = 0.1 T of (a) β-$NaGdF_4$ and (b) β-$NaEuF_4$ particles and (c) hysteresis loops of pure β-$NaEuF_4$ and β-$NaGdF_4$ precursor particles, 22 nm β-$NaGdF_4$ nanocrystals doped with 1% Eu and β-$NaEuF_4$/$NaGdF_4$ core–shell particles at 2 K.

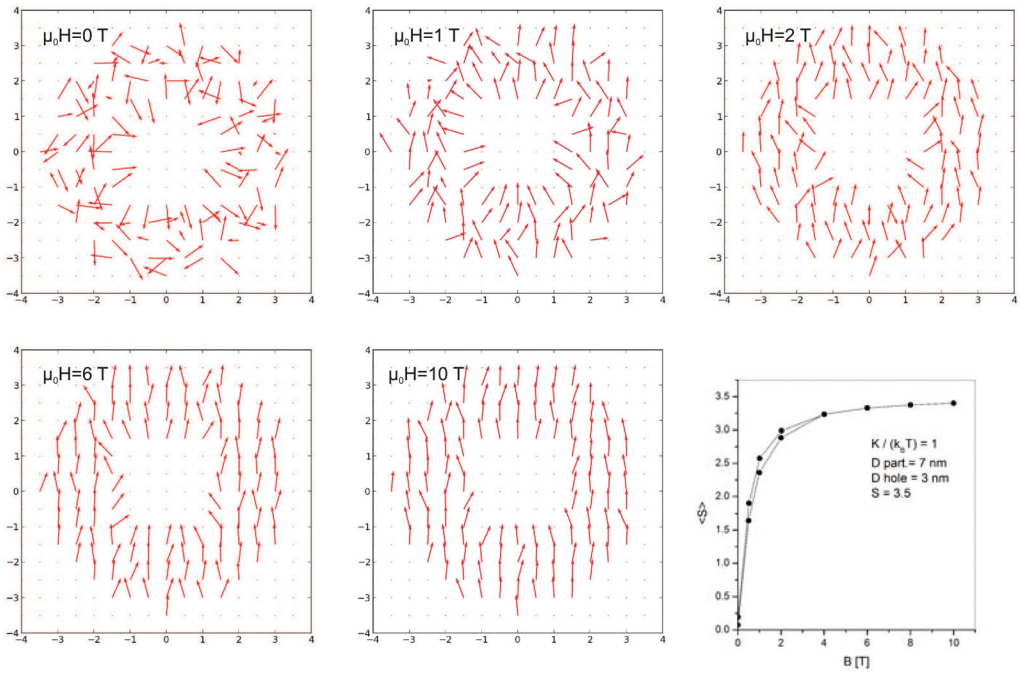

Fig. 9 Spin configurations (central section) for the simulated particles in the fields of 0 T, 1 T, 2 T, 6 T and 10 T (scales in nm) and the simulated hysteresis loops (the first quadrant) for the particle.

described by Ziółkowski and Chrobak.[62] The analyzed particle consists of a spherical magnetic shell (7 nm in diameter) and a nonmagnetic core (3 nm). In the magnetic net, spin S = 3.5, exchange integral parameter J = 0 and radial magnetic anisotropy coefficient $K = k_B T$. Fig. 9 depicts the spin configurations for different applied magnetic fields from 0 T to 10 T.

The resulting average spin in the direction of magnetic field (*i.e.* magnetization of the particle) as a function of increasing and decreasing field is presented in Fig. 9. As shown, this part of simulated hysteresis loop also reveals the butterfly shape. It should be underlined that good qualitative agreement with experimental data could be obtained only with the assumption of the surface anisotropy. The performed simulations including an influence of dipolar interactions, magnetic frustrations, weak ferro and antiferro couplings do not bring satisfactory results. Finally, one can conclude that the magnetization processes of β-$NaGdF_4$ nanoparticles can be affected by anisotropy that leads to the appearing of butterfly shaped hysteresis loops and deviation from the Curie law (see Fig. 8(a)).

In order to tackle the internal magnetic structure of selected β-$NaEuF_4$ and the β-$NaEuF_4$/$NaGdF_4$ core–shell nanocrystals with an 18 nm β-$NaEuF_4$ core in detail we performed X-ray magnetic circular dichroism (XMCD) at the Gd and Eu $M_{4,5}$-edges. XMCD is a very powerful tool to determine the magnetic properties of a compound in question valence and element specific.

Fig. 10 presents the Eu $M_{4,5}$-edge X-ray absorption spectroscopy (XAS) and XMCD spectra of the β-$NaEuF_4$/$NaGdF_4$ core–shell nanocrystals with an 18 nm β-$NaEuF_4$ core along with the Gd M_5-edge of the 2 nm β-$NaGdF_4$ shell. The Gd M_5-edge exhibits a large dichroic signal (~20%) of negative sign and a typical Gd^{3+} multiplet structure.[63]

In contrast the Eu $M_{4,5}$-edge XMCD shows a rather weak negative dichroism of ~2% at the M_5 edge. However, this measured dichroic signal is significantly stronger than expected according to the SQUID data of the pure β-$NaEuF_4$ and β-$NaGdF_4$ nanoparticles. Here the maximum recorded magnetization (see Fig. 8(c)) of the β-$NaEuF_4$ nanocrystals is less than 1% compared to the β-$NaGdF_4$ nanocrystals of same size. Since both, Eu and Gd M_5 exhibit negative signs the net moments are parallelly aligned to each other. Fig. 10(b) displays the Eu $M_{4,5}$-edge XA- and XMCD spectra of the core–shell nanoparticles with those of pure 3 nm β-$NaEuF_4$ nanoparticles. The XPS spectra (see section 2.5) reveal an increased amount of divalent Eu ions which is also reflected in the X-ray absorption- and XMCD spectra of this sample. The M_5 edge XMCD of the 3 nm β-$NaEuF_4$ nanoparticles is dominated by two distinct features located at 1128 eV and 1131 eV, which can be attributed to Eu^{2+} and Eu^{3+} contributions to the XMCD signal.[64] In the case of the core–shell nanocrystals the intensity of the XMCD at 1128 eV is much less pronounced, which is in accordance with the XPS results indicating a significantly lower Eu^{2+} fraction compared to the 3 nm β-$NaEuF_4$ nanoparticles. The XMCD peak at 1132 eV can be presumed as being due to Eu^{3+} ions with a total magnetic quantum number $J \neq 0$, since Eu^{3+} in its magnetic ground state with $J = 0$ would produce no dichroic signal at all. On the other hand, Eu^{2+} ions are in a $J = 7/2$ ground state, leading to a "spin only" moment of $7\mu_B$ per Eu ion. This means that already quite a small fraction of uncompensated moments originating from Eu^{2+} ions may lead to a significant contribution to the overall Eu $M_{4,5}$-edge XCMD signal. As we have already pointed out the overall dichroic Eu signal is much higher than expected from the SQUID magnetometry data. One potential reason is that the Eu^{3+}-signal stems from ions in the $^7F_2$ ($J = 1$) state. This is likely populated *via* the excitation of the probing X-ray beam during the XMCD measurement. Note that 4f intrashell transitions into the $^7F_2$ also dominate the luminescence spectra presented in Fig. 5. A similar effect has been reported by Kachkanov *et al.*[53] for Eu^{3+} doped GaN layers. It seems that

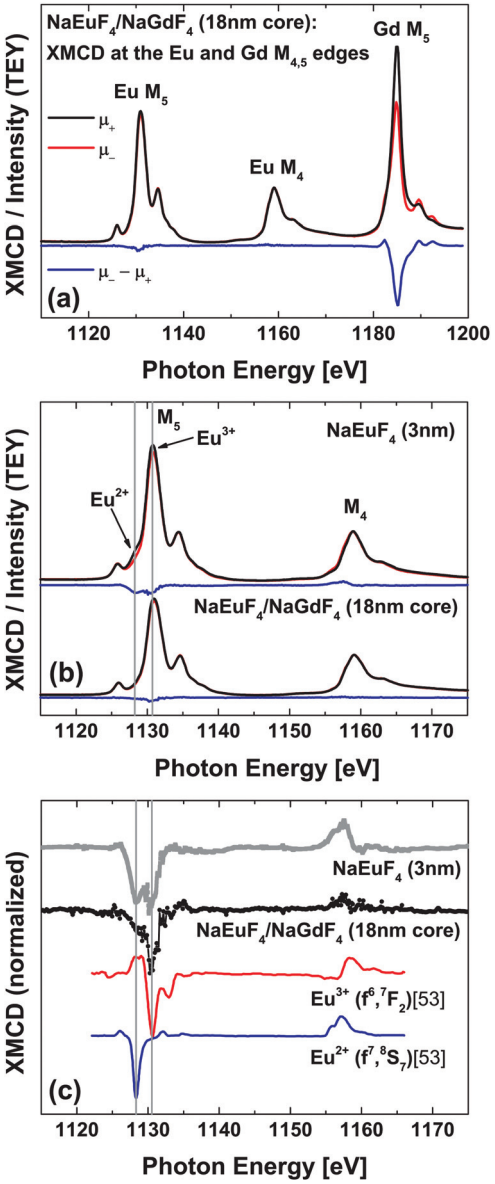

Fig. 10 (a) Gd M_5 and Eu $M_{4,5}$-edge XAS and XMCD of the β-$NaEuF_4$/$NaGdF_4$ core–shell nanocrystals with an 18 nm β-$NaEuF_4$ core. (b) Eu $M_{4,5}$-edge XAS and XMCD of the β-$NaEuF_4$/$NaGdF_4$ core–shell nanocrystals with an 18 nm β-$NaEuF_4$ core and the pure 3 nm β-$NaEuF_4$ nanoparticles. (c) Eu $M_{4,5}$-edge XMCD spectra in comparison with the corresponding atomic multiplet calculations of the $^7F_2$ Eu^{3+} and the $^8S_7$ Eu^{2+} final states. The simulated spectra have been extracted from Kachkanov *et al.*[53] The experiments have been performed under an external magnetic field of $B = 6$ T and with the samples at a temperature of 6 K. Spectra are offset vertically for clarity.

β-$NaEuF_4$ based nanocrystals and core–shell systems could be another example of a material in which the magnetic state can be altered by light excitation. In order to investigate this highly interesting effect in more detail future experiments by means of magneto optical SQUID and/or XMCD measurements in luminescence yield would be desirable.

3 Conclusions

We synthesized β-$NaEuF_4$/$NaGdF_4$ core–shell nanoparticles with narrow size distribution and an overall size of around 22 nm diameter. The particles contained either a small β-$NaEuF_4$ core with a diameter of only ~3 nm or a large β-$NaEuF_4$ core with a diameter of ~18 nm. Structural PDF analysis of the XRD measurements shows differences in peak positions between the both core–shell samples, although the differences in bond distance between the different atoms of bulk β-$NaEuF_4$ and β-$NaGdF_4$ are small. Comparison with simulation based on pure crystalline, spherical β-$NaEuF_4$ and β-$NaGdF_4$ nanoparticles point out that the β-$NaEuF_4$/$NaGdF_4$ core–shell nanoparticle with a 3 nm β-$NaEuF_4$ core exhibits structural parameters of β-$NaGdF_4$ structure, whereas β-$NaEuF_4$/$NaGdF_4$ core–shell nanoparticles with an 18 nm β-$NaEuF_4$ core resemble the β-$NaEuF_4$ structure. HR-TEM images reveal core–shell formation for the β-$NaEuF_4$/$NaGdF_4$ core–shell nanoparticles with an 18 nm β-$NaEuF_4$ core. The Eu^{3+} photoluminescence and Gd^{3+} ESR spectra both indicate that rare earth ions of the small 3 nm particle cores were released during shell growth and incorporate into the shell material. In contrast the system with the large β-$NaEuF_4$ core does not exhibit additional peaks in the Eu^{3+} luminescence spectra indicating that only a small number of Eu^{3+} ions are present in the $NaGdF_4$ shell. As to the Eu and Gd valance states, X-ray photoelectron-core level spectroscopy reveals significant fractions of Eu^{2+} ions in the β-$NaEuF_4$ precursors as well as the β-$NaEuF_4$/$NaGdF_4$ core–shell nanoparticles with an 18 nm β-$NaEuF_4$ core. Larger β-$NaEuF_4$ nanoparticles and surrounded by the β-$NaGdF_4$ shell reduce the Eu^{2+} fraction in agreement with results reported for EuF_3 thin film surfaces and interfaces.[52] The presence of Eu^{2+} in the β-$NaEuF_4$ nanoparticles as well as in the core–shell systems is confirmed by SQUID magnetometry. $M(T)$ curves of the β-$NaEuF_4$ precursors exhibit a sharp increase in magnetization below 20 K stemming from Eu^{2+} ions since only the Eu^{3+} ions contribute a weak van Vleck paramagnetism. In the case of the core–shell system with 3 nm β-$NaEuF_4$ core we find a butterfly-shaped hysteresis loop which is known for single molecular magnets, for instance. This result could be reproduced by Heisenberg model simulations of a magnetic sphere comprising a non-magnetic core. XMCD at the Eu and $M_{4,5}$ edges demonstrates the parallel alignment of Gd and Eu moments in the core–shell nanoparticles with a large β-$NaEuF_4$ core. The magnetic properties are dictated by the paramagnetic Gd^{3+} ions in the surrounding β-$NaGdF_4$ shell. However, both the Eu^{2+} and Eu^{3+} ions contribute to the overall magnetic properties of the system. In particular the Eu^{3+} contribution is much higher than expected from the weak van Vleck paramagnetism. This might be due to the fact that the exciting X-rays populate the $J = 1$ state of Eu^{3+} *via* 4f transitions which can be also seen in the optical spectra. In future studies the core–shell formation with small β-$NaEuF_4$ cores will be further optimized, also to investigate the interesting butterfly shaped magnetic hysteresis in more detail. The fact that the magnetic state of Eu^{3+} might be altered by external light excitation is another interesting aspect which may be investigated by SQUID experiments under optical light excitation or XMCD using luminescence yield as the detection mode. Finally the multifunctionality of the β-$NaEuF_4$/$NaGdF_4$ core–shell nanoparticles could be further improved, *e.g.* by transition metal doping into the β-$NaEuF_4$ core and/or the β-$NaGdF_4$ shell. In summary we have successfully synthesized and carefully characterized multifunctional β-$NaEuF_4$/$NaGdF_4$ core–shell nanoparticles combining intense red optical emission from the Eu^{3+} ions with the paramagnetic properties stemming mainly from the Gd^{3+} ions.

4 Experimental

4.1 Materials

Sodium oleate (82%, Sigma-Aldrich), sodium fluoride (99%, Sigma-Aldrich), ammonium fluoride (98%, Sigma-Aldrich), oleic acid (90%, Alfa Aesar), 1-octadecene (90%, Alfa Aesar) and hydrated rare-earth chlorides of $EuCl_3$ and $GdCl_3$ (99.9%, Treibacher Industrie AG) were used as received.

Rare-earth oleates. The rare-earth oleates were prepared as given in the literature.[65] In a typical synthesis of europium oleate 60 mmol europium chloride and 180 mmol sodium oleate were dispersed in 120 ml ethanol, 80 ml water and 210 ml hexane. The resulting turbid solution was heated for 14 h under reflux (at about 60 °C). The resulting transparent organic phase containing the europium oleate was separated at room temperature and the hexane was removed with a rotary evaporator, yielding europium oleate. Gadolinium oleate was prepared analogously.

Synthesis of cubic phase precursor nanocrystals. The synthesis of the sub-10 nm particles of α-$NaREF_4$ (RE = Eu, Gd) is based on the reaction of rare-earth oleates and NaF in a mixture of oleic acid and 1-octadecene, similar to the procedure given by Liu *et al.*[66] In our case, rare-earth oleate and sodium fluoride were used in a molar ratio of 1 to 8. Oleic acid and 1-octadecene were added to the 1 to 8 mixture of rare-earth oleate and NaF (10 ml of each solvent per 1 mmol of rare-earth oleate) and the mixture was degassed in a vacuum Schlenk-line 100 Pa) for 1 h at 100 °C under stirring. The setup was three times subjected to vacuum and then refilled with nitrogen before the reaction mixture was heated at 200 °C. After 60 min at 200 °C and slow nitrogen flow the stirred solution was allowed to cool to room temperature. The excess of sodium fluoride was removed by centrifugation. The clear supernatant was mixed with an equal volume of ethanol leading to precipitation of the nanoparticles, which were

separated by centrifugation. The particles were purified by redispersing the precipitate in hexane (3 ml hexane per 1 mmol of rare-earth oleate), followed by precipitation with ethanol and separation of the particles by centrifugation.

Synthesis of hexagonal phase precursor nanocrystals. Hexagonal phase precursor particles of $NaREF_4$ were prepared by dispersing the corresponding rare-earth oleate and sodium oleate in a molar ratio of 1 : 2.5 in oleic acid and 1-octadecene (10 ml of each solvent per 1 mmol of rare-earth oleate) followed by degassing at 100 °C for 1 h under vacuum (100 Pa) in a Schlenk-line. Subsequently, 4 mmol ammonium fluoride per 1 mmol of rare-earth oleate was added at 100 °C to the clear yellowish solution under nitrogen flow. The vessel was three times subjected to vacuum and then refilled with nitrogen (vacuum applied for 5 seconds only) and the stirred solution was subsequently heated at 200 °C for 60 min under slow nitrogen flow. After cooling to room temperature an equal volume of ethanol was added to the solution, resulting in precipitation of the precursor particles. The particles were separated by centrifugation and purified as given above for the cubic phase precursor nanocrystals.

Growth of the final product particles. We used a method published earlier by the group of one of the present authors.[67] Product particles with different final sizes were obtained by varying the molar ratio of hexagonal and cubic phase precursor particles. In a typical synthesis, 3.76 mg β-$NaEuF_4$ and 1.28 g α-$NaGdF_4$ precursor particles were re-dispersed in a solvent mixture consisting of 10 ml of oleic acid and 10 ml of 1-octadecene. The mixture was then heated at 100 °C for 60 min under vacuum and stirring. After the vessel was three times subjected to vacuum and then refilled with nitrogen, the solution was heated to 320 °C under nitrogen flow. After the desired reaction time, in this case 40 min, the reaction was stopped and the solution was cooled down to room temperature. After adding 60 ml of a 1 : 2 mixture of hexane and ethanol, the precipitate was separated from the solution by centrifugation. The precipitate was purified two times as given above for the precursor particles. The synthesis procedure for all $NaREF_4$ product particles was the same.

4.2 Experimental methods

The total scattering X-ray measurements were performed on the high energy scattering beamline P02.1 at PETRA III (DESY, Hamburg, Germany). The data sets were collected using a high energy monochromatic beam (59.875 keV, λ = 0.20707 Å) and a Perkin Elmer flat panel detector placed at 303 mm from the samples. The wavelength and the sample to detector distance have been determined by using a LaB_6 NIST standard. The used experimental setup allows to collect total scattering data over a sufficiently high momentum transfer ($Q \sim 22.72$ Å^{-1}) corresponding to a d spacing of 0.138 Å. We note here that the total scattering measurements have been conducted under the same experimental conditions for all the studied samples. The collected data were then corrected for experimental effects (absorption, multiple scattering, polarization, Compton scattering and Laue diffuse scattering) and the scattering signals from the air and the experimental set up were measured independently under exactly the same conditions as the samples and subtracted as a background in the data reduction procedure. For obtaining the experimental atomic pair distribution function $G(r)$ by a direct sine Fourier transformation of the resulting total scattering structure function $S(Q)$, the data were truncated at a finite maximum value of Q_{max} = 18.13 Å^{-1} beyond which the signal-to-noise ratio became unfavourable. All data processing was done using Fit-2D[68] and PDFgetX3[69] software.

A double Cs corrected JEOL ARM 200F transmission electron microscope operated at 200 kV was used for the analysis in the study. High angle annular dark field (HAADF) scanning transmission electron microscopy (STEM) was used along with electron energy loss spectroscopy (EELS) Spectrum Imaging (SI) using the DualEELS™ mode on the Gatan GIF Quantum 965 ERS™ spectrometer fitted on the microscope as well as EDS using an Oxford XMax 80 SDD.

Fluorescence spectra of the nanocrystals were recorded with a Fluorolog 3-22 spectrometer (Jobin Yvon) equipped with double monochromators for both channels.

The EPR spectra of the sample were recorded with a home made X-band EPR spectrometer (9 GHz) equipped with a dielectric resonator (DM5) (Bruker Biospin, Rheinstetten, Germany). The microwave power was set to 1.0 mW, the B-field modulation amplitude was 0.3 mT.

The XPS measurements were performed using a PHI 5600CI multitechnique spectrometer with monochromatic Al Kα = 1486.6 eV radiation of 0.3 eV at full width at half-maximum. The overall resolution of the spectrometer is 1.5% of the pass energy of the analyzer, 0.88 eV in the present case. The XPS measurements were performed at room temperature.

The XAS and XMCD measurements were performed at the Beamline for Advanced Dichroism (BACH) at the Elettra Synchrotron Facility.[70] The samples were mounted into a cryostat equipped with a 6.5 T superconducting magnet, the sample stage was connected to a pumped helium cryostat, reaching a base temperature of around 6.0 K during the experiments presented here. The measurements at the Gd and Eu $M_{4,5}$ edges have been recorded under external magnetic fields of 6 T in the total electron yield mode.

The FC–ZFC and hysteresis loop measurements were performed at the A. Chełkowski Institute of Physics, University of Silesia, Katowice, Poland, with the use of SQUID magnetometer (MPMS XL7 Quantum Design). All measurements have been performed in the 2 K–300 K temperature range up to 7 T magnetic field.

Acknowledgements

Parts of this research were carried out at the light source PETRA III at DESY, a member of the Helmholtz Association (HGF). We would like to thank J. Gamcová for assistance in using beamline P02.1. We thank all Beamline scientists for their excellent and generous technical support.

References

1 S. Gai, C. Li, P. Yang and J. Lin, *Chem. Rev.*, 2014, **114**, 2343–2389.
2 C. Liu, Y. Hou and M. Gao, *Adv. Mater.*, 2014, **26**, 6922–6932.
3 D. K. Chatterjee, M. K. Gnanasammandhan and Y. Zhang, *Small*, 2010, **6**, 2781–2795.
4 F. Wang, D. Banerjee, Y. Liu, X. Chen and X. Liu, *Analyst*, 2010, **135**, 1839–1854.
5 D. Vennerberg and Z. Lin, *Sci. Adv. Mater.*, 2011, **3**, 26–40.
6 O. S. Wolfbeis, *Chem. Soc. Rev.*, 2015, **44**, 4743–4768.
7 Z. Li, Y. Zhang and S. Jiang, *Adv. Mater.*, 2008, **20**, 4765–4769.
8 G. Chen, T. Y. Ohulchanskyy, S. Liu, W.-C. Law, F. Wu, M. T. Swihart, H. Hans Ågren and P. N. Prasad, *ACS Nano*, 2012, **6**, 2969–2977.
9 Q. Liu, Y. Sun, T. Yang, W. Feng, C. Li and F. Li, *J. Am. Chem. Soc.*, 2011, **133**, 17122–17125.
10 J. Liu, Y. Liu, W. Bu, J. Bu, Y. Sun, J. Du and J. Shi, *J. Am. Chem. Soc.*, 2014, **136**, 9701–9709.
11 Y. Sun, X. Zhu, J. Peng and F. Li, *ACS Nano*, 2013, **7**, 11290–11300.
12 Y.-F. Wang, G.-Y. Liu, L.-D. Sun, J.-W. Xiao, J.-C. Zhou and C.-H. Yan, *ACS Nano*, 2013, **7**, 7200–7206.
13 R. Naccache, P. Chevallier, J. Lagueux, Y. Gossuin, S. Laurent, L. Vander Elst, C. Chilian, J. A. Capobianco and M.-A. Fortin, *Adv. Healthcare Mater.*, 2013, **2**, 1478–1488.
14 R. Qiao, C. Liu, M. Liu, H. Hu, C. Liu, Y. Hou, K. Wu, Y. Lin, J. Liang and M. Gao, *ACS Nano*, 2015, **9**, 2120–2129.
15 Y. Deng, H. Wang, W. Gu, S. Li, N. Xiao, C. Shao, Q. Xu and L. Ye, *J. Mater. Chem. B*, 2014, **2**, 1521–1529.
16 H. Groult, J. Ruiz-Cabello, J. Pellico, A. V. Lechuga-Vieco, R. Bhavesh, M. Zamai, E. Almarza, I. Martin-Padura, E. Cantelar, M. P. Martinez-Alcazar and F. Herranz, *Bioconjugate Chem.*, 2015, **26**, 153–160.
17 C. Liu, W. Ma, Z. Gao, J. Huang, Y. Hou, C. Xu, W. Yang and M. Gao, *J. Mater. Chem. C*, 2014, **2**, 9637–9642.
18 R. Wang, X. Li, L. Zhou and F. Zhang, *Angew. Chem., Int. Ed.*, 2014, **126**, 12282–12286.
19 H. Xing, S. Zhang, W. Bu, X. Zheng, L. Wang, Q. Xiao, D. Ni, J. Zhang, L. Zhou, W. Peng, K. Zhao, Y. Hua and J. Shi, *Adv. Mater.*, 2014, **26**, 3867–3872.
20 Q. Zhan, J. Qian, H. Liang, G. Somesfalean, D. Wang, S. He, Z. Zhang and S. Andersson-Engels, *ACS Nano*, 2011, **5**, 3744–3757.
21 D. Yang, P. Ma, Z. Hou, Z. Cheng, C. Li and J. Lin, *Chem. Soc. Rev.*, 2015, **44**, 1416–1448.
22 Y. Dai, H. Xiao, J. Liu, Q. Yuan, P. Ma, D. Yang, C. Li, Z. Cheng, Z. Hou, P. Yang and J. Lin, *J. Am. Chem. Soc.*, 2013, **135**, 18920–18929.
23 Y. I. Park, H. M. Kim, J. H. Kim, K. C. Moon, B. Yoo, K. T. Lee, N. Lee, Y. Choi, W. Park, D. Ling, K. Na, W. K. Moon, S. H. Choi, H. S. Park, S.-Y. Yoon, Y. D. Suh, S. H. Lee and T. Hyeon, *Adv. Mater.*, 2012, **24**, 5755–5761.
24 G. Tian, Z. Gu, L. Zhou, W. Yin, X. Liu, L. Yan, S. Jin, W. Ren, G. Xing, S. Li and Y. Zhao, *Adv. Mater.*, 2012, **24**, 1226–1231.
25 D. Yang, X. Kang, P. Ma, Y. Dai, Z. Hou, Z. Cheng, C. Li and J. Lin, *Biomaterials*, 2013, **34**, 1601–1612.
26 L. Wang, J. Liu, Y. Dai, Q. Yang, Y. Zhang, P. Yang, Z. Cheng, H. Lian, C. Li, Z. Hou, P. Ma and J. Lin, *Langmuir*, 2014, **30**, 13042–13051.
27 R. Naccache, F. Vetrone and J. A. Capobianco, *ChemSusChem*, 2013, **6**, 1308–1311.
28 H. Lian, Z. Hou, M. Shang, D. Geng, Y. Zhang and J. Lin, *Energy*, 2013, **57**, 270–283.
29 J. Shen, Z. Li, R. Cheng, Q. Luo, Y. Luo, Y. Chen, X. Chen, Z. Sun and S. Huang, *ACS Appl. Mater. Interfaces*, 2014, **6**, 17454–17462.
30 G.-B. Shan, H. Assaaoudi and G. P. Demopoulos, *ACS Appl. Mater. Interfaces*, 2011, **3**, 3239–3243.
31 H. Zhu, X. Chen, L. M. Jin, Q. J. Wang, F. Wang and S. F. Yu, *ACS Nano*, 2013, **7**, 11420–11426.
32 Y. Zhou, S.-T. Han, X. Chen, F. Wang, Y.-B. Tang and V. Roy, *Nat. Commun.*, 2014, **5**, 1–8.
33 D. Peng, Q. Ju, X. Chen, R. Ma, B. Chen, G. Bai, J. Hao, X. Qiao, X. Fan and F. Wang, *Chem. Mater.*, 2015, **27**, 3115–3120.
34 W. J. Kim, M. Nyk and P. N. Prasad, *Nanotechnology*, 2009, **20**, 185301.
35 Y. Lu, J. Zhao, R. Zhang, Y. Liu, D. Liu, E. M. Goldys, X. Yang, P. Xi, A. Sunna, J. Lu, Y. Shi, R. C. Leif, Y. Huo, J. Shen, J. A. Piper, J. P. Robinson and D. Jin, *Nat. Photonics*, 2014, **8**, 32–36.
36 J. M. Meruga, A. Baride, W. Cross, J. J. Kellar and P. S. May, *J. Mater. Chem. C*, 2014, **2**, 2221–2227.
37 G.-S. Yi and G.-M. Chow, *Chem. Mater.*, 2007, **19**, 341–343.
38 Y.-F. Wang, L.-D. Sun, J.-W. Xiao, W. Feng, J.-C. Zhou, J. Shen and C.-H. Yan, *Chemistry*, 2012, **18**, 5558–5564.
39 D. Chen and P. Huang, *Dalton Trans.*, 2014, **43**, 11299–11304.
40 G. Chen, H. Agren, T. Y. Ohulchanskyy and P. N. Prasad, *Chem. Soc. Rev.*, 2015, **44**, 1680–1713.
41 M.-K. Tsang, G. Bai and J. Hao, *Chem. Soc. Rev.*, 2015, **44**, 1585–1607.
42 F. Vetrone, R. Naccache, V. Mahalingam, C. G. Morgan and J. A. Capobianco, *Adv. Funct. Mater.*, 2009, **19**, 2924–2929.
43 Y. Liu, D. Tu, H. Zhu, R. Li, W. Luo and X. Chen, *Adv. Mater.*, 2010, **22**, 3266–3271.
44 F. Wang, R. Deng, J. Wang, Q. Wang, Y. Han, H. Zhu, X. Chen and X. Liu, *Nat. Mater.*, 2011, **10**, 968–973.
45 M. Quintanilla, F. Ren, D. Ma and F. Vetrone, *ACS Photonics*, 2014, **1**, 662–669.
46 C. Dong, A. Korinek, B. Blasiak, B. Tomanek and F. C. J. M. van Veggel, *Chem. Mater.*, 2012, **24**, 1297–1305.
47 Q. Su, S. Han, X. Xie, H. Zhu, H. Chen, C.-K. Chen, R.-S. Liu, X. Chen, F. Wang and X. Liu, *J. Am. Chem. Soc.*, 2012, **134**, 20849–20857.

48 H. Wen, H. Zhu, X. Chen, T. F. Hung, B. Wang, G. Zhu, S. F. Yu and F. Wang, *Angew. Chem., Int. Ed.*, 2013, **125**, 13661–13665.
49 X. Li, R. Wang, F. Zhang and D. Zhao, *Nano Lett.*, 2014, **14**, 3634–3639.
50 M. Bottrill, L. Kwok and N. J. Long, *Chem. Soc. Rev.*, 2006, **35**, 557–571.
51 E.-J. Cho and S.-J. Oh, *Phys. Rev. B: Condens. Matter*, 1999, **59**, R15613–R15616.
52 W. Burian, J. Szade, T. O'Keevan and Z. Celinski, *Phys. Status Solidi B*, 2004, **241**, R15–R18.
53 V. Kachkanov, M. J. Wallace, G. van der Laan, S. S. Dhesi, S. A. Cavill, Y. Fujiwara and K. P. O'Donnell, *Sci. Rep.*, 2012, **2**, 1–5.
54 G. H. Dieke, *Spectra and energy levels of rare-earth ions in crystals*, Interscience Publishers, New York, 1968.
55 P. Ptacek, H. Schaefer, K. Koempe and M. Haase, *Adv. Funct. Mater.*, 2007, **17**, 3843–3848.
56 C. Li, Z. Quan, J. Yang, P. Yang and J. Lin, *Inorg. Chem.*, 2007, **46**, 6329–6337.
57 C. M. Brodbeck and L. E. Iton, *J. Chem. Phys.*, 1985, **83**, 4285–4299.
58 R. Komban, J. P. Klare, B. Voss, J. Nordmann, H.-J. Steinhoff and M. Haase, *Angew. Chem., Int. Ed.*, 2012, **51**, 6506–6510.
59 J. Szade and M. Neumann, *J. Phys.: Condens. Matter*, 2001, **13**, 2717.
60 F. Li, C. Li, X. Liu, Y. Chen, T. Bai, L. Wang, Z. Shi and S. Feng, *Chem. – Eur. J.*, 2012, **18**, 11641–11646.
61 L. Margheriti, D. Chiappe, M. Mannini, P.-E. Car, P. Sainctavit, M.-A. Arrio, F. B. de Mongeot, J. C. Cezar, F. M. Piras, A. Magnani, E. Otero, A. Caneschi and R. Sessoli, *Adv. Mater.*, 2010, **22**, 5488–5493.
62 G. Ziółkowski and A. Chrobak, *Acta Phys. Pol., A*, 2015, **127**, 597–598.
63 G. Champion, N. Lalioti, V. Tangoulis, M.-A. Arrio, P. Sainctavit, F. Villain, A. Caneschi, D. Gatteschi, C. Giorgetti, F. Baudelet, M. Verdaguer and C. Cartier dit Moulin, *J. Am. Chem. Soc.*, 2003, **125**, 8371–8376.
64 B. J. Ruck, H. J. Trodahl, J. H. Richter, J. C. Cezar, F. Wilhelm, A. Rogalev, V. N. Antonov, B. D. Le and C. Meyer, *Phys. Rev. B: Condens. Matter*, 2011, **83**, 174404.
65 J. Park, K. An, Y. Hwang, J.-G. Park, H.-J. Noh, J.-Y. Kim, J.-H. Park, N.-M. Hwang and T. Hyeon, *Nat. Mater.*, 2004, **3**, 891–895.
66 C. Liu, H. Wang, X. Zhang and D. Chen, *J. Mater. Chem.*, 2009, **19**, 489–496.
67 B. Voss and M. Haase, *ACS Nano*, 2013, **7**, 11242–11254.
68 A. P. Hammersley, S. O. Svensson, M. Hanfland, A. N. Fitch and D. Hausermann, *High Pressure Res.*, 1996, **14**, 235–248.
69 P. Juhas, T. Davis, C. Farrow and S. Billinge, *J. Appl. Crystallogr.*, 2013, **46**, 560–566.
70 M. Zangrando, M. Finazzi, G. Paolucci, G. Comelli, B. Diviacco, R. P. Walker, D. Cocco and F. Parmigiani, *Rev. Sci. Instrum.*, 2001, **72**, 1313–1319.